The International Journal of Advanced Manufacturing Technology (2022) 122:1679–1694
https://doi.org/10.1007/s00170-022-09944-0

ORIGINAL ARTICLE

# Laser-based powder bed fusion of Ti-6Al-4V powder modified with $SiO_2$ nanoparticles

**Nicole Emminghaus**[1] · **Robert Bernhard**[1] · **Jörg Hermsdorf**[1] · **Stefan Kaierle**[1,2]

Received: 11 April 2022 / Accepted: 10 August 2022 / Published online: 25 August 2022


**Abstract**

In laser-based powder bed fusion of metals (PBF-LB/M), residual oxygen in the processing atmosphere is regarded as disruptive and disadvantageous for the manufacturing process and the resulting component properties. A novel approach to eliminate residual oxygen is to add small amounts of silane to the argon process gas. Silane eliminates residual oxygen and forms $SiO_2$ nanoparticles, which in turn can be incorporated into the powder during the process. It is therefore necessary to evaluate the influence of these nanoparticles admixed to the metal powder. In this work, Ti-6Al-4V powder was modified with pyrogenic $SiO_2$ nanoparticles generated by the reaction of a silane argon gas mixture with ambient air. Modified and unmodified powder was analyzed and processed using statistically designed experiments. An improvement of the flow rate according to DIN EN ISO 4490 (from 33.3 to 32.5 s/50 g) and increase of apparent density according to DIN EN ISO 3923 (from 2.52 to 2.58 g/cm$^3$) could be observed after powder modification. No statistically significant effects of the modification on roughness, porosity, and hardness were found. The results demonstrate that powder modification using silane can lead to enhanced flowability without affecting the PBF-LB processing window of Ti-6Al-4V.

**Keywords** Additive manufacturing · Laser-based powder bed fusion · Ti-6Al-4V · Design of experiments · Powder modification

## 1 Introduction

In many different manufacturing processes, such as grinding, thermal spraying, dry machining, or additive manufacturing (AM), the presence of oxygen in the processing atmosphere is a detrimental and thus undesired factor [1–4]. An innovative approach to eliminate residual oxygen is the application of silane-doped process gases. This approach is currently investigated in the collaborative research center "Oxygen-free production". Silane, also called silicon tetrahydride ($SiH_4$), is a metastable gas that reacts with oxygen and moisture even at room temperature and ambient air pressure. As it can be seen in Eq. 1, the reactants of the reaction are oxygen and silane while pyrogenic, amorphous silicon dioxide (also known as fumed silica) and water are the products of the first reaction. In a second reaction (Eq. 2), the water in turn or already existent moisture in the process atmosphere also reacts with silane and forms silicon dioxide and hydrogen [5, 6].

$$SiH_4(g) + 2O_2(g) \rightarrow SiO_2(s) + 2H_2O(g) \quad (1)$$

$$SiH_4(g) + 2H_2O(g) \rightarrow SiO_2(s) + 4H_2(g) \quad (2)$$

The resulting oxygen partial pressure can reach values of $\leq 10^{-20}$ mbar [6]. Hence, it can be regarded as adequate to extreme high vacuum (XHV) which starts at $10^{-12}$ mbar [7]. The special feature of this approach however, is that the conditions are achieved at normal pressure, which makes expensive vacuum equipment unnecessary. Especially for highly reactive metals like titanium, this approach promises the processing without disruptive oxide layers that normally form immediately when the surface is exposed to atmospheric oxygen. Titanium alloys are one of the most investigated metal materials in additive manufacturing, especially in the laser-based powder bed fusion process (PBF-LB). This processing technology enables the fabrication of highly

✉ Nicole Emminghaus
n.emminghaus@lzh.de

[1] Laser Zentrum Hannover e.V. (LZH), Hollerithallee 8, Hannover D-30419, Germany

[2] Leibniz Universität Hannover, Institut für Transport- und Automatisierungstechnik (ITA), An der Universität 2, Garbsen D-30823, Germany

complex geometries with internal or cellular structures and the economical production of individualized components. It is therefore predestined for the application in medical technology or the manufacturing of topology optimized lightweight components for the aerospace industry [8–10]. The PBF-LB/M processing window for Ti-6Al-4V, the most widely used titanium alloy, has been extensively researched and optimized toward low porosity and surface roughness in the last years [11–15]. Nevertheless, the reproducibility and component quality are limited by internal defects like gas pores or lack of fusion defects as well as oxidation processes that lead to decreased ductility and fatigue strength [16–18]. The application of a silane-doped argon atmosphere in PBF-LB is therefore promising. It could enable higher part qualities and increased reproducibility. The downside of this approach is the formation of $SiO_2$ dust, which is assumed to mix with the powder to be processed. It is not yet known how the formed $SiO_2$ particles affect the processability and component properties. From a different point of view, the inclusion of $SiO_2$ particles in the Ti-6Al-4V powder represents not only a contamination but can also be seen as a powder modification. $SiO_2$ nanoparticles already have a wide range of industrially relevant applications, the most relevant regarding this work is the application as a flow enhancing additive [19]. A well-known industrial product is Aerosil® from Evonik. Multiple applications for the modification of polymeric and metal powders have been reported, e.g., [20–22]. However, the explicit use for metal additive manufacturing has rarely been described in the literature so far. To improve the mixing and in situ alloying of Al-Cu powder mixtures, Karg et al. modified the powder mixture with $SiO_2$ nanoparticles. The stabilization against segregation for small particles < 20 µm led to high homogeneity of the chemical elements in the processed specimens that was also supported by tensile tests [23]. In another work, Karg et al. used drycoating with $SiO_2$ nanoparticles to improve the flowability, measured by the static angle of repose, and layer deposition of Al-Si powder. High relative density of up to 99.97 % and a significant improvement in comparison to uncoated powder containing fine particles < 20 µm were demonstrated [24]. However, potential influences on microstructure and mechanical properties were not addressed in this work. Peng et al. also describe the idea of using nanoparticle dry coating with $SiO_2$ to improve the layer spreading of Ni-based metal powders [25]. Gärtner et al. dry coated equimolar alloy metal powder (CoCrFeNi) with $SiO_2$ nanoparticles to improve its flowability. They observed a reduction of the dynamic angle of repose by 50 % and an increase of the bulk powder density by 30 % [26]. Nevertheless, as the powder was not subsequently processed, it is not known how this modification affects the process and part properties. Insufficient flowability represents a major limitation in the AM of some materials, especially fine powders. Flow improvement by powder modification could thus expand the range of materials that can be processed. Currently, the range of metal powders modified with $SiO_2$ nanoparticles is strongly limited and does not include studies on Ti-6Al-4V. It is therefore unknown how this modification affects the powder flow behavior and the subsequent PBF-LB process. The $SiO_2$ formation under XHV-adequate atmosphere cannot be prevented. It is important to understand how this reaction product can affect the process and if the processing window needs to be adjusted to achieve maximum part quality. The aim of this work is therefore to investigate the processing window for modified Ti-6Al-4V powder and to compare it with that of unmodified powder with regard to roughness, porosity, and hardness. For this purpose, the design of experiments approach is applied and a regression model is set up. In the following, we describe the applied materials and methods as well as the obtained results. Finally, a discussion and a conclusion are given.

## 2 Materials and methods

The methodology can be divided into six substeps: powder modification consisting of $SiO_2$ generation and powder mixing, powder characterization, experimental planning according to the DoE (design of experiments) approach, and the conduction of build jobs as well as specimen characterization as the final step. Figure 1 shows the schematic workflow that was applied in this work. The single steps are described in detail in the following sections.

### 2.1 Powder modification and analysis

The powder material applied in this work was recycled gas atomized Ti-6Al-4V powder (grade 23) supplied by Heraeus Additive Manufacturing GmbH. The virgin powder has a specified particle size of 15–53 µm with a size distribution of D10 = 22 µm, D50 = 38 µm, and D90 = 54 µm according to the manufacturer's datasheet. For the applied recycled powder, the size distribution is more narrow and the mean particle size is slightly higher than for virgin powder [27]. Recycling in this case means that the powder was reused multiple times and sieved with a mesh size of 63 µm after each process. For modification of the powder, a glass container with powder was placed inside a small glovebox (side length of 30 cm) filled with air. In a subsequent step, a gas mixture of argon 5.0 doped with 1 vol% silane was flowed into the glovebox where it reacted with the ambient atmosphere according to Eqs. 1 and 2. During the reaction in the glovebox, no stirring of the powder was applied. After deposition of the $SiO_2$ dust on the powder, the glass container was removed and the powder was manually mixed in a closed container to achieve a homogeneous distribution

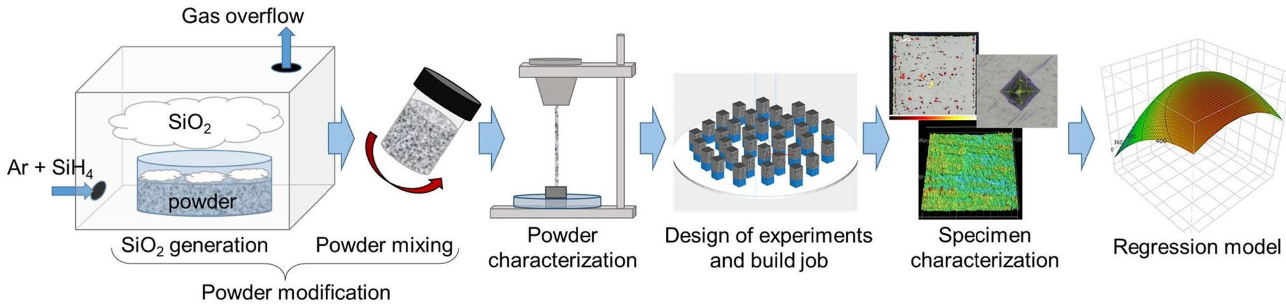


**Fig. 1** Schematic representation of the applied workflow

of the nanoparticles within the powder. The described procedure was chosen instead of admixing commercially available $SiO_2$ nanoparticles (e.g., Aerosil®) with the intention to simulate the powder contamination in the PBF-LB/M process conducted under this silane-doped atmosphere. In this way, it can be ensured that the nanoparticles went through the same formation process and have the same properties. The powder morphology and the homogeneous nanoparticle distribution as well as the nanoparticles themselves were analyzed using scanning electron microscopy (SEM, Quanta 400 FEG, FEI Company) and energy-dispersive X-ray spectroscopy (EDX). The EDX analysis was done with the software EDAX Genesis by AMETEK GmbH. Three SEM pictures of different modified powder particles were further analyzed by image processing with the open-source software Fiji based on ImageJ to estimate the surface coverage of the nanoparticles. For this purpose, first the edge detection was applied to recognize the single nanoparticles. Then, the image was transformed into a binary image, open contours were closed, and subsequently the contours were filled. The processed images were then analyzed using the particle analysis function that calculates the ratio between the white (nanoparticles) and the black areas (underlying host particle surface) which corresponds to the surface coverage. Before additive processing, the flow rate and apparent density were analyzed in accordance with DIN EN ISO 3923 and 4490 using a Hall funnel.

## 2.2 Experimental design and equipment

In order to identify possible influences and interactions of the powder modification on the processing window, it is necessary not only to compare specimens made from modified and unmodified powder, but also to carry out a parameter study for both types of powder. In this way, shifts for optimal parameter combinations with regard to the response variables roughness, porosity and hardness can be identified. An efficient way to minimize the required specimen size while maximizing the obtainable information is the DoE approach. It also enables the description of quantitative relationships, effect sizes, and interactions between the factors (independent variables) and responses (dependent variables) by the derivation of a mathematical model in the form of regression polynomials. In this study, a rotatable central composite design (CCD) with an axial value of $\alpha = 1.682$ was chosen as it allows the evaluation of linear and quadratic effects as well as two-way interactions. The process parameters laser power $P$, scanning speed $v$, and hatch distance $h$ were varied on 5 levels each. The implemented factor levels are given in Table 1 and were chosen based on literature, the authors' experience, and the machine limitations. All parameter combinations given by the chosen design were repeated twice in one build job except the central point, which was repeated 6 times to reduce prediction variance. This led to a total number of 34 specimens per build job. To achieve orthogonality of the experimental design and thus further improve accuracy of prediction, 9 replications of the central point would be necessary but due to limited space on the build platform, this was not feasible. For each type of powder, one build job with the described design was conducted. The build job design is shown in Fig. 2. The parameter combinations were assigned to the specimen IDs in a randomized manner and the specimens were oriented with a 45° angle with respect to the gas flow and recoating direction to minimize position dependent effects. Cubes with a side length of 5 mm on top of 3 mm wall support structures were chosen as specimen geometry. The contour was scanned after the infill but with the same parameters to reduce the number of influencing variables. An offset of 100 µm between infill and contour, a bidirectional scanning strategy with a rotation of 67° between adjacent layers, and a constant layer thickness $t$ of 30 µm were implemented. No platform heating was applied. An overview of all specimen IDs with the respective parameter settings can be found in the appendix (Table 6).

The response values of interest in this study are porosity $\phi$, top surface roughness $S_{a_{Top}}$, side surface roughness $S_{a_{Side}}$,

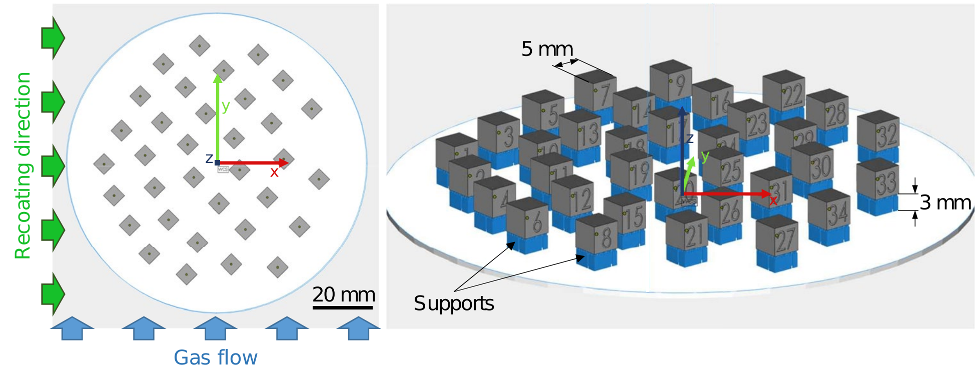


**Fig. 2** Implemented build job layout with direction of gas flow, recoating movement, and engraved specimen IDs

and hardness $H$. To evaluate the factor effects on these responses, a mathematical model was fitted using the least squares method. To reduce heteroscedasticity, all responses except the hardness were transformed using log-transformation. For the statistical analysis, a significance level of 5 % ($p$-value > 0.05) was chosen. Effects with larger $p$-values were excluded from the model following the principle of strong effect heredity. This means that the effect can only be excluded when there is no significant dependent higher order effect left in the model. The generation of the experimental design as well as the statistical analysis of the experimental data was conducted using the statistics software JMP®(SAS Institute Inc.). The experiments were carried out on an industrial machine, TruPrint 1000 by Trumpf GmbH & Co. KG (Ditzingen, Germany), that is equipped with a 200-W ytterbium fiber laser (single mode, continuous wave, wavelength 1070 nm). It enables a minimum spot diameter of 30 µm that is created by a telecentric f-theta lens. A minimum residual oxygen content of 200 ppm was maintained using high purity argon as a process gas.

## 2.3 Specimen characterization

The specimens were manually removed from the build platform and subsequently examined for their roughness by employing optical profilometry (OP). For all specimens, the side surface opposite to the engraved number and the top surface were analyzed using the confocal laser scanning microscope VK-X1000 series with

**Table 1** Levels of the varied processing parameters according to the central composite design

| Parameter | Levels | | | | |
|---|---|---|---|---|---|
| Laser power (W) | 115 | 145 | 175[c] | 205 | 235 |
| Scanning speed (mm/s) | 600 | 800 | 1000[c] | 1200 | 1400 |
| Hatch spacing ($\mu$m) | 40 | 60 | 80[c] | 100 | 120 |

[c]Center point parameter combination

a VK-X1100 measurement unit (semiconductor laser with wavelength of 404 nm, height display resolution of 0.5 nm) by Keyence. The repeatability of the employed objective lens in combination with the laser confocal height measurement is 0.1 µm (1-sigma) and the accuracy is given by Eq. 3.

$$Accuracy = 1 + \frac{measurement\ length\,(\mu m)}{100\ \mu m} \tag{3}$$

The arithmetic mean roughness ($S_a$) based on a square area with a side length of 2 mm was used as the characteristic value for the roughness. $S_a$ was chosen instead of its linear corollary $R_a$ because different studies suggest that $R_a$ is not sufficient to describe the surface topology of additively manufactured parts [28]. Selected specimens were further examined using SEM and EDX to investigate possible $SiO_2$ residuals on the surface. After surface characterization, all specimens were cold embedded in epoxy resin (Technovit Epox, Kulzer GmbH, Hanau, Germany), ground with SiC abrasive paper, and polished with OP-S solution (Tegramin, Struers ApS, Ballerup, Denmark). For every specimen, three cross-sections were made parallel to the build direction (BD) and analyzed with the light microscopy function of the VK-X1000 microscope. Using a Python script developed at Laser Zentrum Hannover e.V. (LZH), the stitched microscopic images were first transformed to black and white with a given threshold value and in a subsequent calculation of the proportion of black and white pixels the porosity was determined. For the statistical evaluation, only the mean porosity of the three cross-sections per specimen was used. On the last cross-section of each specimen, the Vickers hardness HV0.1 was measured with an indentation time of 10 s (INNOVATEST NEXUS 4000 testing machine). Three indentations located halfway up the specimen, starting at 0.75 mm distance to the side surface and continuing towards the middle with a step size of 0.75 mm, were conducted. Additionally, the cross-sections were etched using Kroll's reagent and the microstructure was analyzed using light microscopy and EDX mapping.

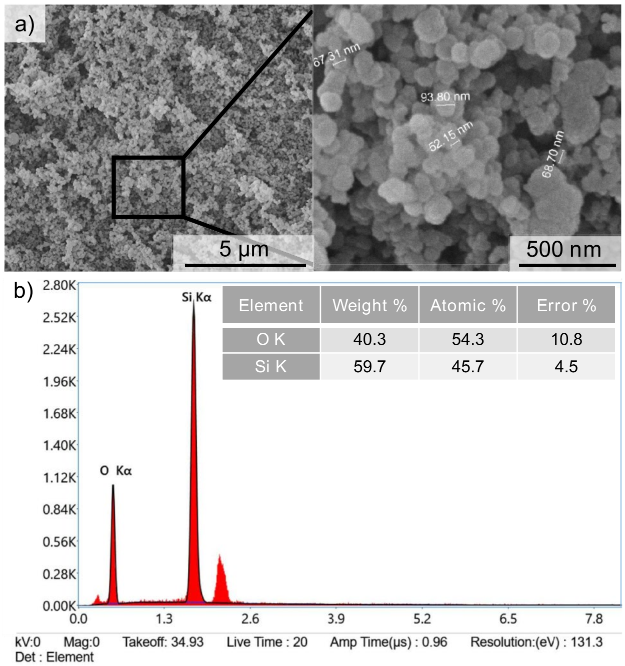


**Fig. 3** $SiO_2$ dust collected from the glovebox: **a** SEM images of the agglomerated nanoparticles with sizes between 50 and 100 nm; **b** EDX analysis confirming the chemical composition of the $SiO_2$ nanoparticles

# 3 Results

## 3.1 Powder

Collected $SiO_2$ dust from the glovebox was analyzed regarding the nanoparticle size and chemical composition. Single nanoparticles show sizes ranging between 50 and 100 nm and are mainly forming larger agglomerates (Fig. 3a). The EDX analysis confirms the composition of oxygen and silicon (Fig. 3b).

Modified and unmodified powders were also analyzed using SEM. The SEM images (Fig. 4) show that the Ti-6Al-4V powder has a mainly spherical morphology with a smooth particle surface. Only few satellites were observed beneath the larger particles, what can be attributed to the coarsening effect of powder recycling [27]. Regarding the modified powder, a homogeneous distribution of the $SiO_2$ nanoparticles on the surface of the Ti-6Al-4V host particles was observed. The nanoparticles were evenly distributed on all powder particles and no larger agglomerates of the $SiO_2$ particles could be seen. In general, the particles on the SEM images all had a similar coverage with $SiO_2$ nanoparticles; therefore, a homogeneous dispersion is assumed. The image processing and analysis using Fiji revealed a surface coverage between 14 and 17 %. The flow rate was evaluated in accordance with DIN EN ISO 4490. For unmodified Ti-6Al-4V, a mean flow rate of 33.3 s/50 g was obtained while the modification with $SiO_2$ nanoparticles led to a mean flow rate of 32.5 s/50 g, an improvement by 3.4 %. Additionally, the apparent density was measured according to DIN EN ISO 3923. Here an increase from 2.51 g/cm³ for unmodified to 2.58 g/cm$^3$ for modified powder, an increase by 2.8 %, could be observed. The results of the flowability characterization are summarized in Table 2. The statistical analysis showed a significant influence of the powder modification on the flow rate ($p = 0.0139$) and on the apparent density ($p < 0.0001$). The $r^2$-value for the regression of the flow rate ($r^2 = 0.81$) was smaller than the one for the apparent density ($r^2 = 0.99$), which can be explained by the different standard deviations (Table 2).

## 3.2 Surface characterization

The surface roughness was investigated on the top as well as on the side surface of the cube specimens. For the top surface roughness, a maximum of 51.7 µm ($P = 130$ W, $v = 1000$ mm/s, $h = 60$ µm, unmodified powder) and a minimum of 7.8 µm ($P = 170.2$ W, $v = 700$ mm/s, $h = 80$ µm, modified powder) were observed. For the side surface roughness, the maximum was 33.5 µm ($P = 145$ W, $v = 195.5$ mm/s, $h = 80$ µm, modified powder) and the minimum was 8.1 µm ($P = 145$ W, $v = 700$ mm/s, $h = 80$ µm, unmodified powder). Figure 5 displays the height profiles of the top and side surfaces for the center point parameter setting. No differences in surface topography can be observed between modified and unmodified powder.

A multiple linear regression and statistical analysis were conducted after log-transformation of the responses to reduce heteroscedasticity. Only laser power and scanning speed had a significant influence on top and side surface roughness (Table 3). No significant effect could be observed for the hatch distance and the powder modification. For both types of roughness, also quadratic and cubic as well as two-way interaction effects were found to be statistically significant. The quadratic effect of scanning speed in the case of the top surface roughness and the linear effects of laser power and scanning speed in the case of the side surface roughness were left in the model although they have $p$-values of $> 0.05$. This is due to the principle of strong effect heredity explained in Sect. 2.2. The contour plots visualize the evaluated processing map (Fig. 6). With increasing scanning speed and decreasing laser power, the top surface roughness increases. For the side surface roughness, a minimum can be achieved for medium laser power and scanning speed while the roughness increases with decreasing scanning speed. Due to high variance of the roughness values on both surfaces, the $r^2$-values of the regression models were relatively low with $r^2 = 0.44$ for the top surface and $r^2 = 0.46$ for the side surface. The prediction expressions are given in the appendix.

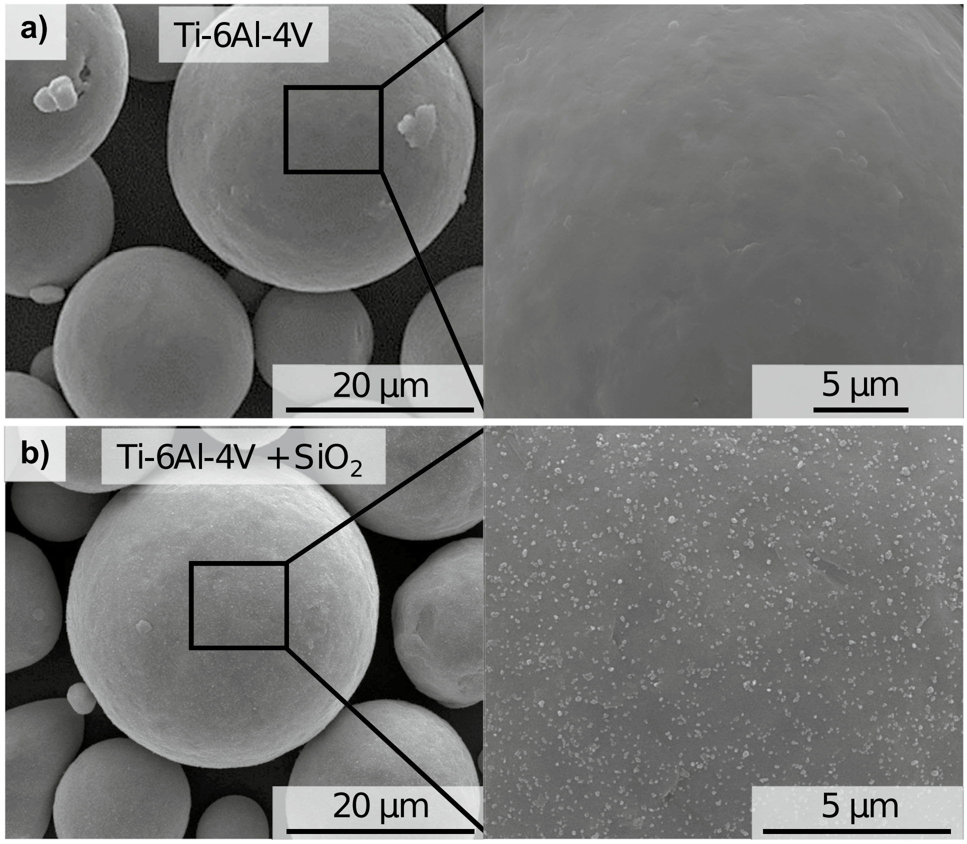


**Fig. 4** SEM images of Ti-6Al-4V powder: **a** unmodified powder, **b** modified powder with $SiO_2$ nanoparticles

Besides optical profilometry, also SEM (Fig. 7) and EDX were used to characterize the as-built surface. On the side surface, sintered and partly melted particles were visible. The top surface showed the partly overlapping scan paths and some smaller particles that have their origin in spattering and the balling effect. The SEM images did not show any $SiO_2$ particles left on the as-built surface made of the modified powder (Fig. 7).

### 3.3 Porosity

Across all experiments, a minimum porosity of 0.03 % ($P$ = 160 W, $v$ = 1000 mm/s, $h$ = 60 µm, unmodified) and a maximum porosity of 5.30 % ($P$ = 130 W, $v$ = 1000 mm/s, $h$ = 100 µm, modified) were obtained. The quadratic effect of the scanning speed had the strongest influence on the porosity followed by the interaction of laser power and scanning speed. The hatch distance also had a significant but smaller effect. The interactions between hatch distance and the two other varied process parameters were all significant (Table 4). No significant effect of the powder modification was observed. The contour plot (Fig. 8) shows the dependency of the porosity on the two most influential factors, scanning speed and laser power. A low porosity can be achieved for medium to high laser power at medium scanning speed of 700 mm/s. From this point on, the porosity increases for increasing as well as decreasing scanning speed. The regression model has an $r^2$-value of 0.69. The prediction expression can be found in the appendix.

### 3.4 Hardness

Regarding the hardness, a maximum of 445.7 HV0.1 ($P$ = 145 W, $v$ = 195.5 mm/s, $h$ = 80 µm, unmodified) and a minimum of 349.0 HV0.1 ($P$ = 130 W, $v$ = 1000 mm/s, $h$ = 100 µm, modified) were observed. The powder modification

**Table 2** Results of standardized powder characterization according to DIN EN ISO 4490 and 3923

| Characteristic | | Ti-6Al-4V | Ti-6Al-4V + $SiO_2$ |
|---|---|---|---|
| Flow rate (s/50 g) | Mean | 33.3 | 32.5 |
| | Standard deviation | 0.2 | 0.3 |
| Apparent density (g/cm$^3$) | Mean | 2.51 | 2.58 |
| | Standard deviation | 0.01 | < 0.01 |

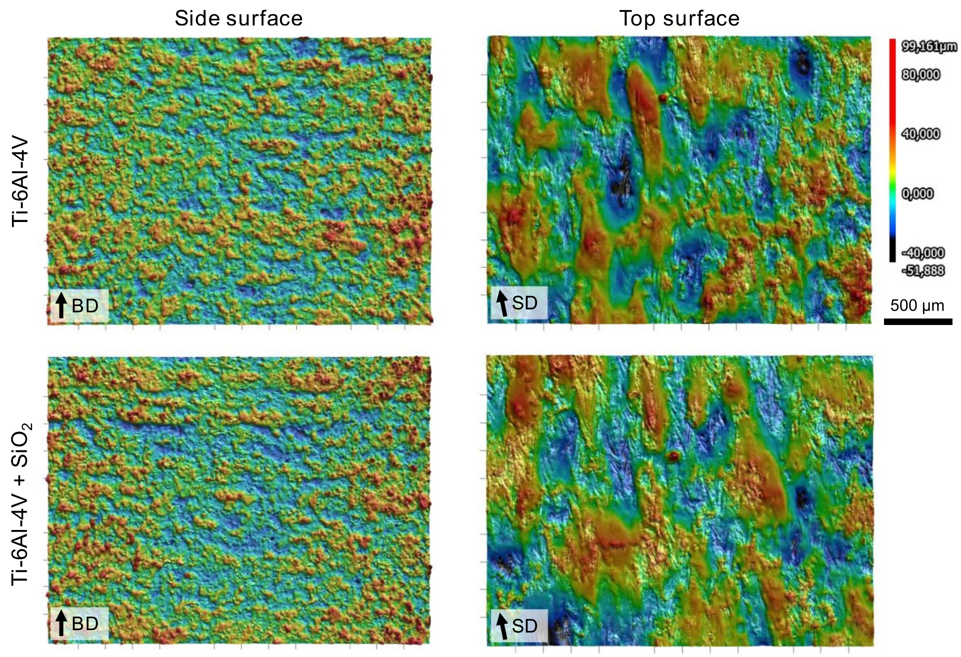


**Fig. 5** Height profiles of the side and top surfaces for unmodified and modified powder and for the center point parameter setting; build direction (BD) and scan direction (SD) indicated by arrows

did not show a significant influence. The hardness was significantly influenced by the three process parameters scanning speed, laser power, and hatch distance. Thereby, the scanning speed and the hatch distance showed the largest effect sizes and the lowest *p*-values (Table 5). With increasing hatch distance and scanning speed, the hardness decreases (Table 5, Fig. 9). For the laser power, there is a setting for maximum hardness that depends on the setting of the scanning speed, as there is a significant interaction between these factors. For medium scanning speed of 700 mm/s, a maximum hardness can be obtained for a medium laser power of 145 W (Fig. 9). The goodness-of-fit for the regression model of hardness is $r^2 = 0.47$. The prediction expression based on the estimates is given in the appendix.

**Table 3** Parameter estimates of the regression model for the top and side surface roughness after log-transformation

| Term | Estimate | Std. error | *t*-value | *p*-value |
|---|---|---|---|---|
| Top surface | | | | |
| Intercept | 2.5741 | 0.0468 | 55.04 | < 0.0001 |
| Scanning speed | 0.3509 | 0.0843 | 4.16 | < 0.0001 |
| Laser power · scanning speed | −0.1601 | 0.0502 | −3.19 | 0.0023 |
| Laser power | −0.1561 | 0.0384 | −4.06 | 0.0001 |
| Scanning speed$^2$ | −0.1127 | 0.0427 | −2.64 | 0.0104 |
| Scanning speed$^3$ | 0.0097 | 0.0394 | 0.25 | 0.8063 |
| Side surface | | | | |
| Intercept | 2.2950 | 0.0479 | 47.94 | < 0.0001 |
| Scanning speed$^2$ | 0.1623 | 0.0315 | 5.15 | < 0.0001 |
| Laser power · scanning speed | −0.0890 | 0.0392 | −2.27 | 0.0264 |
| Laser power$^2$ | 0.0820 | 0.0315 | 2.60 | 0.0116 |
| Scanning speed$^3$ | −0.0801 | 0.0332 | −2.41 | 0.0190 |
| Scanning speed | 0.0369 | 0.0657 | 0.56 | 0.5758 |
| Laser power | −0.0025 | 0.0299 | −0.08 | 0.9351 |

## 3.5 Microstructure

To investigate possible effects of the powder modification on the microstructure, etched cross-sections were analyzed. There were no noticeable differences between specimens made of unmodified and modified powder, as exemplarily shown for different applied volume energy densities in Fig. 10. In both cases, a fine microstructure with prior-$\beta$-grains oriented in build direction (BD) and $\alpha$'-martensite needles oriented at 45° to the $\beta$-grains were observed (Fig. 10). With increasing energy input, a coarsening of the microstructure with larger prior-$\beta$-grains was observed. For parameter combinations that lead to massive overheating, as for $E_V = 309.1$ J/mm$^3$ in Fig. 10, the prior-$\beta$-grains become less oriented. Additionally, the observed martensite needles are smaller. For each powder type, four selected cross-sections were also analyzed using EDX measurements. On one sample per powder type, additionally an EDX mapping was performed. No significant differences in silicon content could be detected in the EDX measurements (Appendix Table 7). Since the oxygen content measured for the cross-sections was below the minimum detection limit, no inferences on differences in oxygen content can be made. The EDX mappings were comparable for both powder types and

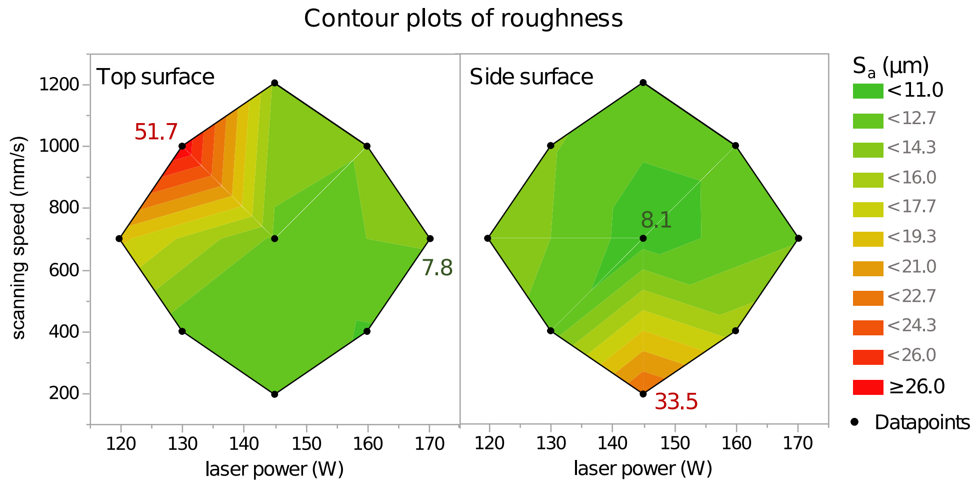


**Fig. 6** Contour plot of the top and side surface roughness depending on the factors scanning speed and laser power. The colors indicate the roughness from small values (green) to high values (red). Maximum and minimum values are marked

displayed a homogeneous elemental distribution (Appendix Fig. 13).

## 4 Discussion

This research focused on the effect of $SiO_2$ nanoparticle modification of Ti-6Al-4V powder on the PBF-LB process. Therefore, the powder was characterized in a standardized manner and subsequently, the response variables top and side surface roughness, porosity, and hardness as well as the microstructure were evaluated. It was found that the powder modification leads to a reduced flow rate and thus a better flowability as well as an increased apparent density. On the other side, no significant effect of the powder modification on the processing window and part properties was observed. The improved flowability was also described in other works on powder modification, e.g., [23–26]. By covering the host particle surfaces, the nanoparticles on the one hand increase the apparent roughness and thus the distance between two particles. As a consequence, the Van-der-Waals forces between the particles are reduced [26]. On the other hand,

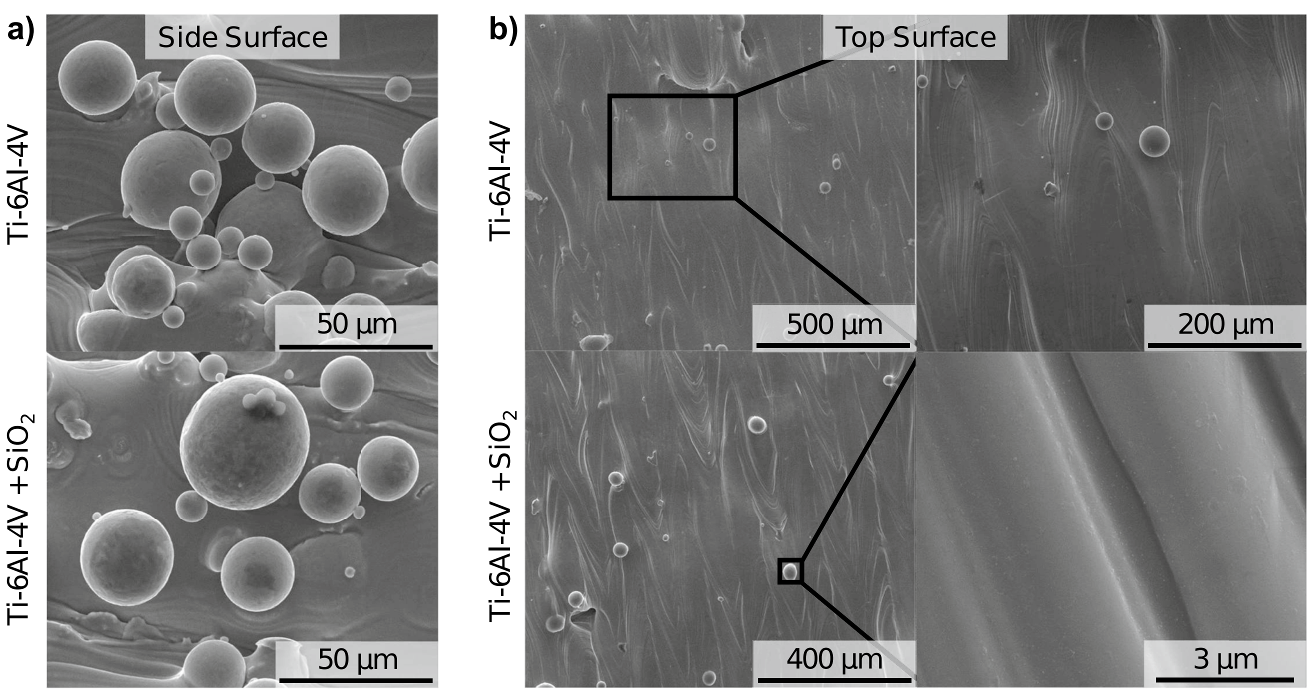


**Fig. 7** SEM images of as-built surfaces for both types of powder: **a** side surface with sintered particles, **b** top surface with visible scan tracks and without remaining $SiO_2$ particles on the surface

**Table 4** Parameter estimates of the regression model for porosity after log-transformation

| Term | Estimate | Std. error | *t*-value | *p*-value |
|---|---|---|---|---|
| Intercept | −1.8816 | 0.1604 | −11.73 | < 0.0001 |
| Scanning speed$^2$ | 0.7526 | 0.1055 | 7.14 | < 0.0001 |
| Laser power · scanning speed | −0.5827 | 0.1310 | −4.45 | < 0.0001 |
| Laser power | −0.5779 | 0.1003 | −5.76 | < 0.0001 |
| Scanning speed · hatch distance | 0.4149 | 0.1310 | 3.17 | 0.0024 |
| Laser power$^2$ | 0.3276 | 0.1055 | 3.11 | 0.0029 |
| Hatch distance | 0.2867 | 0.1003 | 2.86 | 0.0059 |
| Laser power · hatch distance | 0.2649 | 0.1310 | 2.02 | 0.0478 |
| Scanning speed | −0.0849 | 0.1003 | −0.85 | 0.4005 |

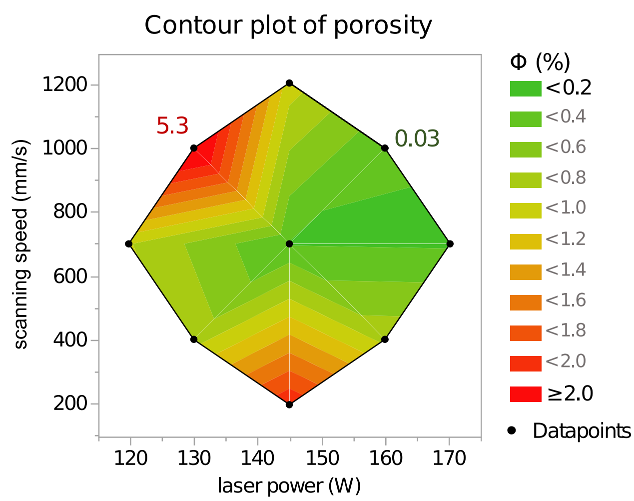


**Fig. 8** Contour plot of the porosity depending on the factors scanning speed and laser power. The colors indicate the porosity from small values (green) to high values (red). Maximum and minimum values are marked

the nanoparticles act as ball bearings between the larger host particles and therefore enhance flow [19]. Another aspect is the formation of liquid brides which also plays an important role in cohesive behavior of powders [29]. Yang et al. for example attributed the observed improvement of flowability after modification with hydrophobized nanosilica to the reduction of liquid bridges [30]. Figure 11 illustrates these mechanisms.

As stated by Gärtner et al. the concentration and size of the nanoparticles are an important criteria [26]. The amount of surface coverage of 14–17 % in this study is in the range of 10–20 % for which other studies achieved optimal fluidization [31–33]. While other types of nanoparticles like carbon black, $Al_2O_3$ or SiC used to modify powder for additive manufacturing led to significant changes in laser absorption [34, 35] or mechanical properties [36], the application of $SiO_2$ particles in this work did not show influences regarding these aspects. This can be attributed to differences in the melting and boiling points of the different nanoparticle materials as well as different influences on the laser absorption. $Al_2O_3$ and SiC used in other studies [35, 36] provide melting and boiling points significantly higher than that of $SiO_2$ (1713 °C and 2200 °C, respectively)[37]. Consequently, they can form inclusions in the built parts and lead to changes of the mechanical properties. When it comes to powder modification to achieve specific powder and part properties, the added nanoparticles should therefore be chosen based on the desired effects on flowability, mechanical properties, and melting behavior. $SiO_2$ particles seem to be suitable for flow improvements without significantly affecting mechanical properties and the required energy input. However, as powder in general has a higher laser absorption than bulk material due to multiple reflections in the powder bed [38], it is possible that small changes of the powder surface structure due to modification are not noticeable. Future research will therefore include absorption measurements using an integrating sphere. In contrast to powder

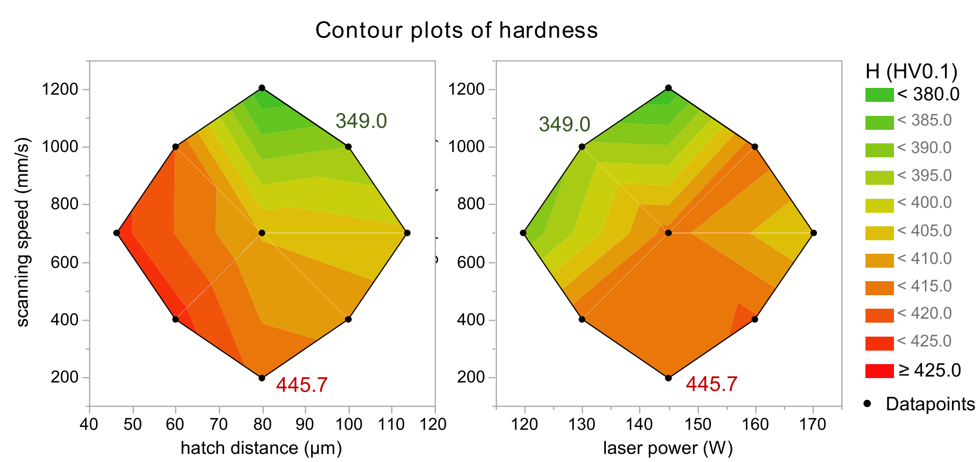


**Fig. 9** Contour plot of the hardness depending on the factors scanning speed, hatch distance, and laser power. The colors indicate the hardness from small values (green) to high values (red). Maximum and minimum values are marked

**Table 5** Parameter estimates of the regression model for hardness

| Term | Estimate | Std. error | *t*-value | *p*-value |
|---|---|---|---|---|
| Intercept | 414.0361 | 3.2323 | 128.09 | < 0.0001 |
| Scanning speed | −8.3912 | 2.0218 | −4.15 | 0.0001 |
| Hatch distance | −8.2953 | 2.0218 | −4.10 | 0.0001 |
| Laser power · scanning speed | 5.3438 | 2.6416 | 2.02 | 0.0475 |
| Laser power$^2$ | −5.1552 | 2.1260 | −2.42 | 0.0183 |
| Laser power | 5.0632 | 2.0218 | 2.50 | 0.0150 |
| Scanning speed$^2$ | −4.6102 | 2.1260 | −2.17 | 0.0340 |

modification, the process parameters laser power, scanning speed, and hatch distance showed significant effects. These effects can partly be explained by taking the volume energy density $E_V$ into account, given by Eq. 4.

$$E_V = \frac{P}{v \cdot h \cdot t} \tag{4}$$

Other works have shown a dependence of the roughness on the volume energy density [39–42] that can also be confirmed in this work. With decreasing scanning speed and increasing laser power, $E_V$ also increases. This leads to larger melt pools and increased sintering of particles on the side surface [41, 43]. Consequently, the side surface roughness increases. With increasing scanning speed and decreasing laser power, $E_V$ decreases. Below a certain threshold, the energy introduced is no longer sufficient to melt the powder completely. Due to insufficient melting and high melt viscosity, discontinuous melt tracks are generated and a high top surface roughness results [44]. This in turn is related to the formation of lack-of-fusion (LoF) defects that lead to increased porosity [45]. This correlation of porosity and roughness and the influence of the melting behavior was also shown by Wang et al. [40]. In our work, it was shown that a high porosity is obtained either for low (high scanning speed, low laser power) or high volume energy density (low scanning speed, high laser power). These two areas of high porosity correspond to different types of pores. While the mentioned LoF defects occur for low energy input [45], spherical gas pores, also known as keyhole pores, are generated when the energy input is too high so that overheating and evaporation take place [46, 47]. The interaction effect of laser power and scanning speed showed a strong and significant effect in all regression models. In contrast to the roughness models, the models for porosity and hardness additionally contained significant effects of the hatch distance. As with the scanning speed, the volume energy density is inversely proportional to the hatch distance (Eq. 4). A decreasing $E_V$ due to increasing hatch distance results in insufficient melting of the powder and therefore increased porosity. Furthermore, with increasing hatch distance and scanning speed, the hardness decreases. Regarding the laser power, the hardness can be reduced either for low or for high values. The hardness decrease for low volume energy density is likely to be attributed to the insufficient melting of the powder and the

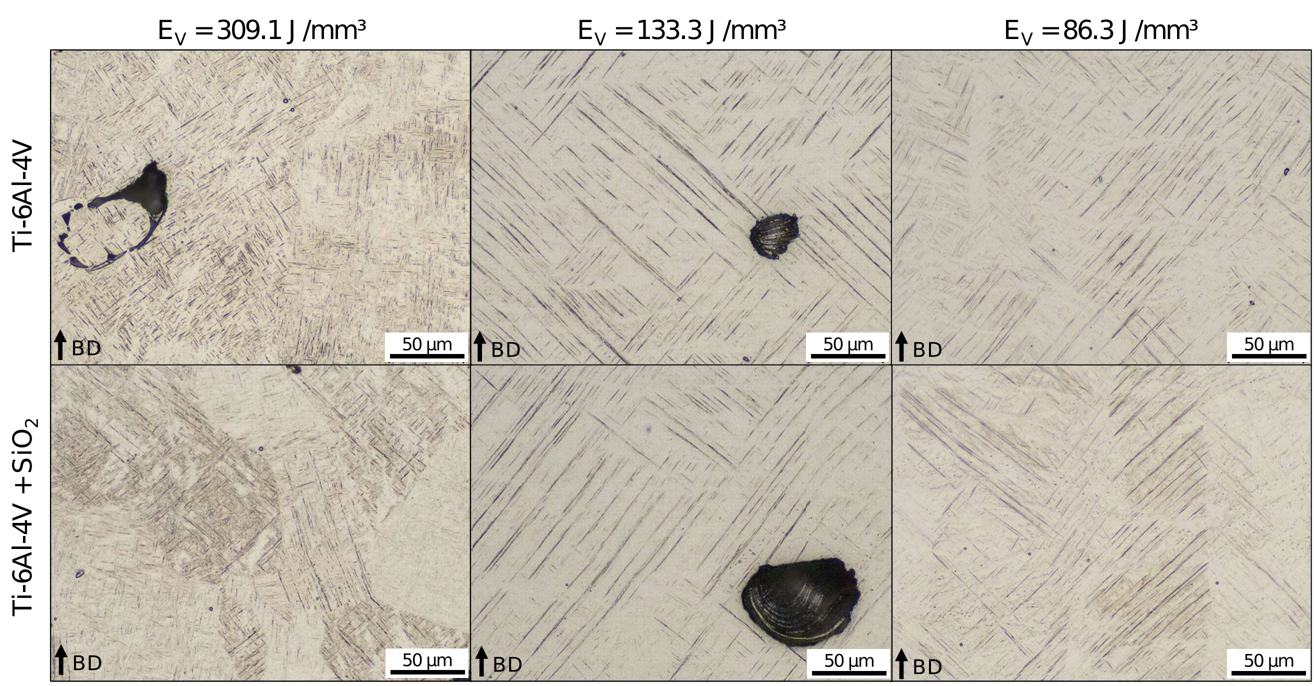


**Fig. 10** Cross-section of specimens etched with Krolls reagent showing the typical fine martensitic microstructure; build direction (BD) is indicated by an arrow

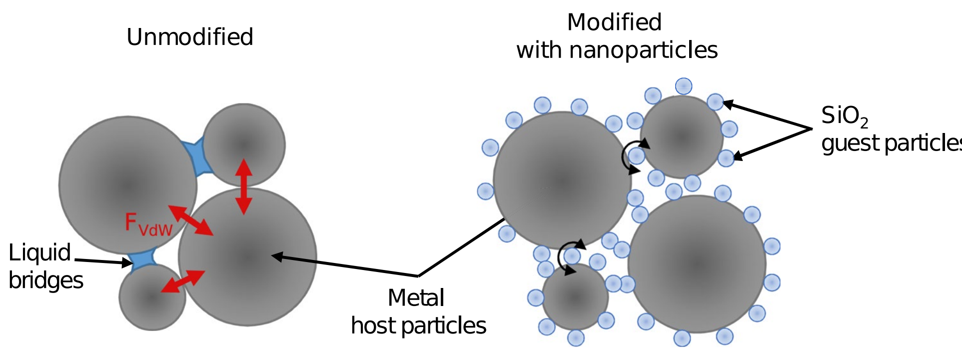


**Fig. 11** Interparticulate mechanisms with liquid bridges and Van-der-Waals forces ($F_{VdW}$) impeding flow of unmodified powders and $SiO_2$ nanoparticles acting as ball bearings and flow promoters in modified powder

resulting LoF defects. Similar effects were also reported in the literature [48–51]. When the volume energy input is high enough to cause evaporation and keyhole pores, larger melt pools are obtained resulting in slower solidification, grain coarsening, and therefore a decrease in hardness. All presented regression models, except the one for porosity, showed a medium goodness-of-fit slightly below $r^2 = 0.5$. There is consequently a high proportion of variation in the experimental data that cannot be explained by the models. This is attributed to the high variance inherent to the PBF-LB process that is not fully understood and under control yet. There is a high number of influencing factors and it is not possible to include all of them in a regular study. Accordingly, the observed variance could be explained by irregularities in the gas flow, powder deposition, or inhomogeneity of beam intensity across the build platform [52–54]. It is also important to mention that the models are only applicable in the investigated parameter range and transferability to other machine set-ups or other materials is limited. Besides the effects of the $SiO_2$ nanoparticles on the process, it is also of interest how the nanoparticles are affected during the PBF-LB process. Since no nanoparticles were found on the specimens' surfaces, it is assumed that they were partly incorporated into the melt and to another part evaporated during the process. A removal by the inert gas flow is rather unlikely. A sample of the unmelted powder was taken after the build-process finished and was analyzed using SEM. The particles were still covered by nanoparticles without a visible change in the amount or distribution. Additionally, no agglomerates of the fine powder could be observed. Therefore, a homogeneous chemical distribution can be assumed in the built part, as it was supported by the EDX mappings. Although the carriage of smaller powder particles by the gas flow takes place during processing and is regarded as one reason for coarsening of recycled powder [55, 56], it is assumed that this is not the case for the nanoparticles adhering to the host particle surfaces. An indicator for melt incorporation would be a change in microstructure and mechanical properties as observed in other works [36, 57–59]. Silicon acts as a beta stabilizer and promotes grain refinement [60, 61]. When the solubility of silicon in titanium is exceeded, silicides are formed. The silicides improve the creep resistance but can also have negative effects on the mechanical properties [62]. Taking into account the high temperatures and cyclic reheating during the process, incorporated $SiO_2$ nanoparticles can react with the surrounding titanium matrix. The silicon then forms silicides with the titanium while the oxygen diffuses into the titanium matrix [63]. However, changes in microstructure, chemical composition, or hardness could not be observed in this study. Nevertheless, it is possible that the used amount of nanoparticles was too small to lead to significant changes in microstructure and hardness. To evaluate this hypothesis in depth, further investigations, especially tensile tests and more detailed microstructure analysis, will be necessary. Since this work focused on the processing window and the parameter influences on porosity and roughness of the as built specimens, a thorough study of the microstructure and depending mechanical properties will be part of future studies. Attention should also be paid to the anisotropy typical of additively manufactured components [64] and to what extent dissolved $SiO_2$ nanoparticles have an influence on this. A limitation of this study is that there was no fixed mixing ratio of powder and nanoparticles. The applied method to generate $SiO_2$ nanoparticles was meant to simulate the $SiO_2$ generation in a PBF-LB process under silane-induced XHV-adequate atmosphere. In order to give an indication of the amount of $SiO_2$ produced, Eq. 5 was used, which is based on the calculations by Holländer et al. [6]. Holländer et al. calculated the mass flow of formed $SiO_2$ due to a constant value of residual oxygen in an open system. In the present case, the flooded machine represents a closed system with a defined initial amount of residual oxygen. The calculation is therefore reduced to the formed mass of $SiO_2$ $m_{SiO_2}$ in dependence of the regarded gas volume $V_{gas}$, the contained oxygen $x_{O_2}$, and moisture amount $x_{H_2O}$ in this volume under the prerequisite of a temperature of 20 °C and an ambient pressure of 1013 mbar.

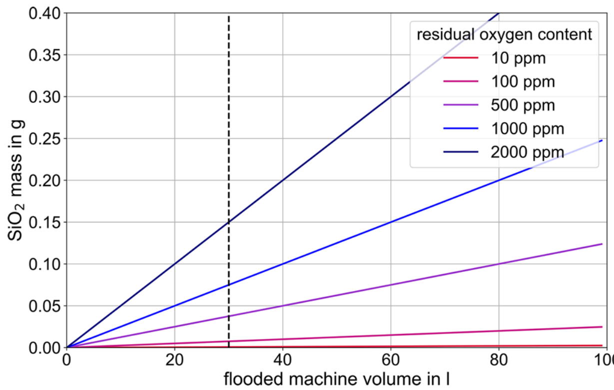


**Fig. 12** Formed $SiO_2$ mass as a function of the flooded machine volume and the residual oxygen (20 °C, 1013 mbar, residual moisture neglected). The vertical line indicates the test chamber volume of 30 l that was considered in this work

$$\frac{m_{SiO_2}}{g} = 2.5 \cdot 10^{-6} \cdot \frac{V_{gas}}{l} \cdot \left( \frac{x_{O_2}}{ppm} + \frac{1}{2} \frac{x_{H_2O}}{ppm} \right) \quad (5)$$

The generated $SiO_2$ mass in dependence of different residual oxygen contents was plotted against the regarded machine volume (Fig. 12). Residual moisture was neglected for this calculation. The volume of 30 l of the test chamber described in this work is marked by a vertical line. The machine, in which the XHV-adequate atmosphere will be generated, will be flooded with argon first to already reduce the residual oxygen content as much as possible. Therefore, the plot only displays residual oxygen contents that are realistic for PBF-LB machines. The $SiO_2$ mass increases linearly with increasing residual oxygen content and increasing flooded machine volume. The residual oxygen content must therefore already be reduced to a minimum before silane is added in order to keep the formation of dust to a minimum. In this work, the silane content of 1 vol-% was the limiting factor instead of the residual oxygen content, because no prior flooding with argon took place. It becomes clear that this is a very conservative approach and that significantly less $SiO_2$ will be produced in the real process. Nevertheless, the formed $SiO_2$ could accumulate in the powder when it is reused multiple times.

In the future, on the one hand, different concentrations should be tested in order to be able to make quantitative statements about the influence of the nanoparticles. The powder should be investigated after different amounts of reusing cycles, so that a possible accumulation of $SiO_2$ after multiple build jobs can be quantified. Furthermore, the chemical composition of the Ti-6Al-4V particles will be investigated after different numbers of build jobs. It is assumed that under silane-doped argon atmosphere the oxidation of the powder during processing is reduced. Regarding the mixing process, possible segregation and agglomeration processes should also be taken into account. They might lead to chemical inhomogeneity in the built part. In addition, it is expected that the dust could not only have an effect in the powder but also in the atmosphere before it settles. Here, the laser radiation can be scattered and thus the energy input can be weakened. This in turn can affect the process window. It is therefore essential to carry out experiments in an XHV-adequate atmosphere, which is now planned as part of the ongoing collaborative research center. An innovative system has already been built for this purpose [4]. For the specific application of the PBF-LB process in a silane-induced XHV-adequate atmosphere, the described results indicate that the expected formation of $SiO_2$ nanoparticles and their infiltration of the powder is likely to not affect the processing window. In a more general view, the findings indicate that by modifying powders with $SiO_2$ nanoparticles their flowability can be improved while maintaining the established parameter settings. Consequently, it is possible to process a wider range of powder materials and achieve a broader spectrum of properties for additively manufactured parts.

## 5 Conclusion

In this work, the influence of $SiO_2$ nanoparticle modification of Ti-6Al-4V powder on the powder flowability and the PBF-LB process was investigated. The following conclusions can be drawn:

- Powder modification with $SiO_2$ nanoparticles led to an improvement in flowability, characterized by a reduced flow rate (from 33.3 to 32.5 s/50 g) and an increased apparent density (from 2.52 to 2.58 g/cm$^3$).
- Powder modification had no significant effect on top and side surface roughness, porosity, hardness, or visible microstructure.
- Roughness and porosity were mostly influenced by laser power and scanning speed while scanning speed and hatch distance had the strongest effects on hardness.
- All regression models showed a significant influence of the two-way interaction of laser power and scanning speed, which can be explained by the resulting volume energy density.
- Powder modification with $SiO_2$ nanoparticles is an effective measure to increase flowability and therefore achieve a wider range of processable powder materials while maintaining the processing window.

Future research will include tensile tests and in-depth microstructural analysis using X-ray diffraction (XRD) as well as experiments under silane-induced XHV-adequate atmosphere.

## Appendix

### Prediction expression for top surface roughness $S_{a_{Top}}$

$$\frac{S_{a_{Top}}}{\mu m} = exp\Bigg(2.5741 - 0.1561 \cdot \left(\frac{P - 145W}{15W}\right) + 0.3510 \cdot \left(\frac{v - 700\frac{mm}{s}}{300\frac{mm}{s}}\right) - 0.1601 \cdot \left(\left(\frac{P - 145W}{15W}\right) \cdot \left(\frac{v - 700\frac{mm}{s}}{300\frac{mm}{s}}\right)\right) + 0.0097 \cdot \left(\frac{v - 700\frac{mm}{s}}{300\frac{mm}{s}}\right)^2 - 0.1127 \cdot \left(\frac{v - 700\frac{mm}{s}}{300\frac{mm}{s}}\right)^3\Bigg) \quad (6)$$

### Prediction expression for side surface roughness $S_{a_{Side}}$

$$\frac{S_{a_{Side}}}{\mu m} = exp\Bigg(2.2950 - 0.0025 \cdot \left(\frac{P - 145W}{15W}\right) + 0.0369 \cdot \left(\frac{v - 700\frac{mm}{s}}{300\frac{mm}{s}}\right) - 0.0890 \cdot \left(\left(\frac{P - 145W}{15W}\right) \cdot \left(\frac{v - 700\frac{mm}{s}}{300\frac{mm}{s}}\right)\right) + 0.0820 \cdot \left(\frac{P - 145W}{15W}\right)^2 + 0.1623 \cdot \left(\frac{v - 700\frac{mm}{s}}{300\frac{mm}{s}}\right)^2 - 0.0801 \cdot \left(\frac{v - 700\frac{mm}{s}}{300\frac{mm}{s}}\right)^3\Bigg) \quad (7)$$

### Prediction expression for porosity $\phi$

$$\frac{\phi}{\%} = exp\Bigg(-1.8816 - 0.5779 \cdot \left(\frac{P - 145W}{15W}\right) - 0.0849 \cdot \left(\frac{v - 700\frac{mm}{s}}{300\frac{mm}{s}}\right) + 0.2867 \cdot \left(\frac{h - 80\mu m}{20\mu m}\right) - 0.5827 \cdot \left(\left(\frac{P - 145W}{15W}\right) \cdot \left(\frac{v - 700\frac{mm}{s}}{300\frac{mm}{s}}\right)\right) + 0.2649 \cdot \left(\left(\frac{P - 145W}{15W}\right) \cdot \left(\frac{h - 80\mu m}{20\mu m}\right)\right) + 0.4149 \cdot \left(\left(\frac{v - 700\frac{mm}{s}}{300\frac{mm}{s}}\right) \cdot \left(\frac{h - 80\mu m}{20\mu m}\right)\right) + 0.3276 \cdot \left(\frac{P - 145W}{15W}\right)^2 + 0.7526 \cdot \left(\frac{v - 700\frac{mm}{s}}{300\frac{mm}{s}}\right)^2\Bigg) \quad (8)$$

### Prediction expression for hardness $H$

$$\frac{H}{HV0.1} = 414.0361 + 5.0632 \cdot \left(\frac{P - 145W}{15W}\right) - 8.3912 \cdot \left(\frac{v - 700\frac{mm}{s}}{300\frac{mm}{s}}\right) - 8.2953 \cdot \left(\frac{h - 80\mu m}{20\mu m}\right) - 5.1552 \cdot \left(\frac{P - 145W}{15W}\right)^2 + 5.3438 \cdot \left(\left(\frac{P - 145W}{15W}\right) \cdot \left(\frac{v - 700\frac{mm}{s}}{300\frac{mm}{s}}\right)\right) - 4.6102 \cdot \left(\frac{v - 700\frac{mm}{s}}{300\frac{mm}{s}}\right)^2 \quad (9)$$

**Table 6** Specimen IDs with corresponding parameter settings

| Specimen ID | Laser power (W) | Scanning speed (mm/s) | Hatch distance (µm) |
|---|---|---|---|
| 1 | 145.0 | 700.0 | 80.0 |
| 2 | 170.2 | 700.0 | 80.0 |
| 3 | 145.0 | 1204.5 | 80.0 |
| 4 | 145.0 | 195.5 | 80.0 |
| 5 | 160.0 | 400.0 | 100.0 |
| 6 | 145.0 | 700.0 | 80.0 |
| 7 | 145.0 | 700.0 | 80.0 |
| 8 | 130.0 | 1000.0 | 60.0 |
| 9 | 145.0 | 700.0 | 80.0 |
| 10 | 160.0 | 1000.0 | 100.0 |
| 11 | 130.0 | 1000.0 | 100.0 |
| 12 | 130.0 | 1000.0 | 100.0 |
| 13 | 130.0 | 400.0 | 60 |
| 14 | 145.0 | 700.0 | 113.6 |
| 15 | 170.2 | 700.0 | 80.0 |
| 16 | 145.0 | 700.0 | 80.0 |
| 17 | 145.0 | 700.0 | 113.6 |
| 18 | 160.0 | 1000.0 | 60.0 |
| 19 | 130.0 | 1000.0 | 60.0 |
| 20 | 160.0 | 400.0 | 60.0 |
| 21 | 130.0 | 400.0 | 60.0 |
| 22 | 145.0 | 700.0 | 46.4 |
| 23 | 130.0 | 400.0 | 100.0 |
| 24 | 119.8 | 700.0 | 80.0 |
| 25 | 119.8 | 700.0 | 80.0 |
| 26 | 160.0 | 400.0 | 100.0 |
| 27 | 160.0 | 1000.0 | 60.0 |
| 28 | 160.0 | 400.0 | 60.0 |
| 29 | 145.0 | 700.0 | 46.4 |
| 30 | 160.0 | 1000.0 | 100.0 |
| 31 | 145.0 | 1204.5 | 80.0 |
| 32 | 145.0 | 195.5 | 80.0 |
| 33 | 130.0 | 400.0 | 100.0 |
| 34 | 145.0 | 700.0 | 80.0 |

**Table 7** Si content in EDX analysis of selected cross-sections

| Specimen ID | Powder | Si content (wt-%) | Minimum detection limit | Si content (at-%) | Error (%) |
|---|---|---|---|---|---|
| 4 | Unmodified | 0.4 | 0.08 | 0.7 | 11.1 |
| 5 | Unmodified | 0.5 | 0.08 | 0.7 | 11 |
| 9 | Unmodified | 0.4 | 0.08 | 0.7 | 11.1 |
| 11 | Unmodified | 0.5 | 0.08 | 0.8 | 11.1 |
| 4 | Modified | 0.5 | 0.08 | 0.8 | 11 |
| 5 | Modified | 0.5 | 0.08 | 0.8 | 10.3 |
| 9 | Modified | 0.5 | 0.08 | 0.8 | 12.1 |
| 11 | Modified | 0.5 | 0.08 | 0.8 | 11.7 |

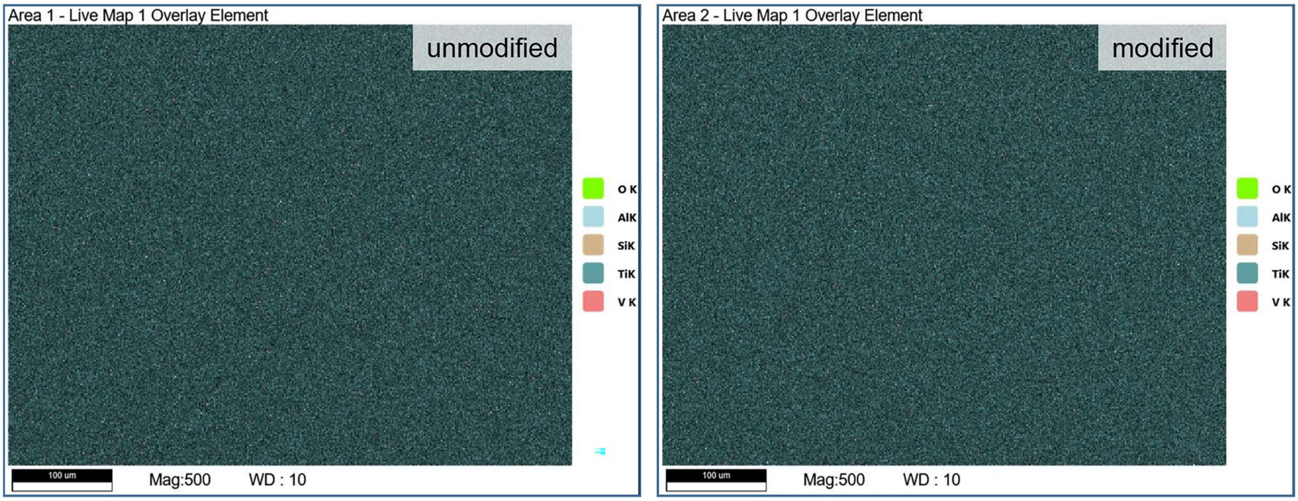


**Fig. 13** EDX mappings of specimens made of unmodified and modified powder, center point parameter setting

**Author contribution** Nicole Emminghaus: conception, execute trials, analysis, interpretation, visualization, writing — original draft preparation. Robert Bernhard: writing — review and editing, supervision. Jörg Hermsdorf: writing — review and editing, supervision. Stefan Kaierle: writing — review and editing, supervision.

**Funding** Open Access funding enabled and organized by Projekt DEAL. Funded by the Deutsche Forschungsgemeinschaft (DFG, German Research Foundation) — Project-ID 394563137 — SFB 1368.

**Availability of data and material** The data is stored in the CKAN repository of the SFB 1368 and is available upon request.

**Code availability** Not applicable.

## Declarations

**Conflict of interest** The authors declare no competing interests.



## References


1. Schaper F, Denkena B, Dittrich MA, Krödel A, Matthies J, Worpenberg S (2021) Wear behaviour of PCBN, PCD, binderless PCBN and cemented carbide cutting inserts when machining Ti-6Al-4V in an oxygen-free atmosphere. In: Behrens BA, Brosius A, Hintze W, Ihlenfeldt S, Wulfsberg JP (eds) Production at the leading edge of technology, Springer, Berlin, Heidelberg, pp 275–283. https://doi.org/10.1007/978-3-662-62138-7_28
2. Rodriguez Diaz M, Nicolaus M, Möhwald K, Maier HJ (2021) Thermal spraying in silane-doped shielding gases: a new approach for innovative coatings in controlled process atmospheres. Thermal Spray Bulletin 14:120–127
3. Maier HJ, Herbst S, Denkena B, Dittrich MA, Schaper F, Worpenberg S, Gustus R, Maus-Friedrichs W (2020) Towards dry machining of titanium-based alloys: a new approach using an oxygen-free environment. Metals 10(9):1161. https://doi.org/10.3390/met10091161, https://www.mdpi.com/2075-4701/10/9/1161
4. Emminghaus N, Fritsch S, Büttner H, August J, Tegtmeier M, Huse M, Lammers M, Hoff C, Hermsdorf J, Kaierle S (2021) PBF-LB/M process under a silane-doped argon atmosphere: preliminary studies and development of an innovative machine concept. Advances in Industrial and Manufacturing Engineering 2:100040. https://doi.org/10.1016/j.aime.2021.100040,https://www.sciencedirect.com/science/article/pii/S2666912921000106
5. Tamanini F, Chaffee JL, Jambor RL (1998) Reactivity and ignition characteristics of silane/air mixtures. Process Saf Prog 17(4):243–258. https://doi.org/10.1002/prs.680170405, https://onlinelibrary.wiley.com/doi/abs/10.1002/prs.680170405
6. Holländer U, Wulff D, Langohr A, Möhwald K, Maier HJ (2020) Brazing in SiH4-doped inert gases: a new approach to an environment friendly production process. Int J Pr Eng Man-GT 7(6):1059–1071. https://doi.org/10.1007/s40684-019-00109-1, https://doi.org/10.1007/s40684-019-00109-1
7. Redhead PA (1999) Extreme high vacuum. Proc Cern Accel Sch Snekersten, Denmark, Cern Report, Ed by STurn pp 213–224
8. Dzogbewu TC (2020) Laser powder bed fusion of Ti6Al4V lattice structures and their applications. J Met Mater Miner 30(4):68–78
9. Vignesh M, Ranjith Kumar G, Sathishkumar M, Manikandan M, Rajyalakshmi G, Ramanujam R, Arivazhagan N (2021) Development of biomedical implants through additive manufacturing: a review. J Mater Eng Perform 30(7):4735–4744. https://doi.org/10.1007/s11665-021-05578-7, https://doi.org/10.1007/s11665-021-05578-7
10. Blakey-Milner B, Gradl P, Snedden G, Brooks M, Pitot J, Lopez E, Leary M, Berto F, du Plessis A (2021) Metal additive manufacturing in aerospace: a review. Mater Des 209:110008. https://doi.org/10.1016/j.matdes.2021.110008, https://www.sciencedirect.com/science/article/pii/S0264127521005633

11. Cepeda-Jiménez CM, Potenza F, Magalini E, Luchin V, Molinari A, Pérez-Prado MT (2020) Effect of energy density on the microstructure and texture evolution of Ti-6Al-4V manufactured by laser powder bed fusion. Mater Charact 163:110238. https://doi.org/10.1016/j.matchar.2020.110238, https://www.sciencedirect.com/science/article/pii/S1044580319326063
12. Gordon JV, Narra SP, Cunningham RW, Liu H, Chen H, Suter RM, Beuth JL, Rollett AD (2020) Defect structure process maps for laser powder bed fusion additive manufacturing. Addit Manuf 36:101552. https://doi.org/10.1016/j.addma.2020.101552, https://www.sciencedirect.com/science/article/pii/S2214860420309246
13. Shipley H, McDonnell D, Culleton M, Coull R, Lupoi R, O'Donnell G, Trimble D (2018) Optimisation of process parameters to address fundamental challenges during selective laser melting of Ti-6Al-4V: a review. Int J Mach Tools Manuf 128:1–20. https://doi.org/10.1016/j.ijmachtools.2018.01.003, https://www.sciencedirect.com/science/article/pii/S0890695518300233
14. Khorasani AM, Gibson I, Ghasemi A, Ghaderi A (2019) A comprehensive study on variability of relative density in selective laser melting of Ti-6Al-4V. Virtual Phys Prototyp 14(4):349–359. https://doi.org/10.1080/17452759.2019.1614198, https://doi.org/10.1080/17452759.2019.1614198
15. Li Z, Kucukkoc I, Zhang DZ, Liu F (2018) Optimising the process parameters of selective laser melting for the fabrication of Ti6Al4V alloy. Rapid Prototyp J 24(1):150–159. https://doi.org/10.1108/RPJ-03-2016-0045, https://doi.org/10.1108/RPJ-03-2016-0045
16. Dietrich K, Diller J, Dubiez-Le Goff S, Bauer D, Forêt P, Witt G (2020) The influence of oxygen on the chemical composition and mechanical properties of Ti-6Al-4V during laser powder bed fusion (L-PBF). Addit Manuf 32:100980. https://doi.org/10.1016/j.addma.2019.100980, https://www.sciencedirect.com/science/article/pii/S2214860419309583
17. Vrancken B, Buls S, Kruth JP, Van Humbeeck J (2015) Influence of preheating and oxygen content on selective laser melting of Ti6Al4V. In: Proceedings of the 16th RAPDASA Conference
18. Velasco-Castro M, Hernández-Nava E, Figueroa IA, Todd I, Goodall R (2019) The effect of oxygen pickup during selective laser melting on the microstructure and mechanical properties of Ti-6Al-4V lattices. Heliyon 5(12):e02813. https://doi.org/10.1016/j.heliyon.2019.e02813, https://www.sciencedirect.com/science/article/pii/S2405844019364734
19. Barthel H, Rösch L, Weis J (2005) Fumed silica-production, properties, and applications. From Molecules to Materials, Organosilicon Chemistry Set, pp 761–778
20. Berretta S, Ghita O, Evans KE (2014) Morphology of polymeric powders in laser sintering (LS): from polyamide to new PEEK powders. Eur Polym J 59:218–229. https://doi.org/10.1016/j.eurpolymj.2014.08.004, https://www.sciencedirect.com/science/article/pii/S0014305714002808
21. Blümel C, Sachs M, Laumer T, Winzer B, Schmidt J, Schmidt M, Peukert W, Wirth KE (2015) Increasing flowability and bulk density of PE-HD powders by a dry particle coating process and impact on LBM processes. Rapid Prototyp J 21(6):697–704. https://doi.org/10.1108/RPJ-07-2013-0074, https://doi.org/10.1108/RPJ-07-2013-0074
22. Melnichuk M, Cuscueta DJ, Silin N (2018) Effect of glidants on LaNi5 powder flowability. Int J Hydrog Energy 43(12):6219–6228. https://doi.org/10.1016/j.ijhydene.2018.01.207, https://www.sciencedirect.com/science/article/pii/S0360319918303628
23. Karg MC, Rasch M, Schmidt K, Spitzer SA, Karsten TF, Schlaug D, Biaciu CR, Gorunov AI, Schmidt M (2018) Laser alloying advantages by dry coating metallic powder mixtures with SiOx nanoparticles. Nanomaterials 8(10):862
24. Karg MCH, Munk A, Ahuja B, Backer MV, Schmitt JP, Stengel C, Kuryntsev SV, Schmidt M (2019) Expanding particle size distribution and morphology of aluminium-silicon powders for laser beam melting by dry coating with silica nanoparticles. J Mater Process Technol 264:155–171. https://doi.org/10.1016/j.jmatprotec.2018.08.045, https://www.sciencedirect.com/science/article/pii/S092401361830387X
25. Peng W, Wang G, Gigliotti Jr MFX, Singh P (2018) Method for treating powder by dry mixing and powder treated thereby. US Patent 9,994,716
26. Gärtner E, Jung HY, Peter NJ, Dehm G, Jägle EA, Uhlenwinkel V, Mädler L (2021) Reducing cohesion of metal powders for additive manufacturing by nanoparticle dry-coating. Powder Technol 379:585–595. https://doi.org/10.1016/j.powtec.2020.10.065, https://www.sciencedirect.com/science/article/pii/S0032591020310159
27. Santecchia E, Spigarelli S, Cabibbo M (2020) Material reuse in laser powder bed fusion: side effects of the laser-metal powder interaction. Metals 10(3):341. https://doi.org/10.3390/met10030341, https://www.mdpi.com/2075-4701/10/3/341
28. Whip B, Sheridan L, Gockel J (2019) The effect of primary processing parameters on surface roughness in laser powder bed additive manufacturing. Int J Adv Manuf Technol 103(9):4411–4422. https://doi.org/10.1007/s00170-019-03716-z
29. Sharma R, Setia G (2019) Mechanical dry particle coating on cohesive pharmaceutical powders for improving flowability - a review. Powder Technol 356:458–479. https://doi.org/10.1016/j.powtec.2019.08.009, https://www.sciencedirect.com/science/article/pii/S0032591019306084
30. Yang J, Sliva A, Banerjee A, Dave RN, Pfeffer R (2005) Dry particle coating for improving the flowability of cohesive powders. Powder Technol 158(1):21–33. https://doi.org/10.1016/j.powtec.2005.04.032, https://www.sciencedirect.com/science/article/pii/S0032591005001531
31. Huang Q, Zhang H, Zhu J (2010) Flow properties of fine powders in powder coating. Particuology 8(1):19–27. https://doi.org/10.1016/j.partic.2009.05.007, https://www.sciencedirect.com/science/article/pii/S1674200109001692
32. Han M, Zhou Y, Zhu J (2020) Improvement on flowability and fluidization of Group C particles after nanoparticle modification. Powder Technol 365:208–214. https://doi.org/10.1016/j.powtec.2019.07.026, https://www.sciencedirect.com/science/article/pii/S0032591019305182
33. Xu CC, Zhang H, Zhu J (2009) Improving flowability of cohesive particles by partial coating on the surfaces. Can J Chem Eng 87(3):403–414. https://doi.org/10.1002/cjce.20179, https://onlinelibrary.wiley.com/doi/abs/10.1002/cjce.20179
34. Jadhav SD, Dadbakhsh S, Vleugels J, Hofkens J, Van Puyvelde P, Yang S, Kruth JP, Van Humbeeck J, Vanmeensel K (2019) Influence of carbon nanoparticle addition (and impurities) on selective laser melting of pure copper. Materials 12(15):2469. https://doi.org/10.3390/ma12152469, https://www.mdpi.com/1996-1944/12/15/2469
35. Pannitz O, Großwendt F, Lüddecke A, Kwade A, Röttger A, Sehrt JT (2021) Improved process efficiency in laser-based powder bed fusion of nanoparticle coated maraging tool steel powder. Materials 14(13):3465. https://doi.org/10.3390/ma14133465, https://www.mdpi.com/1996-1944/14/13/3465
36. Sehrt JT, Kleszczynski S, Notthoff C (2017) Nanoparticle improved metal materials for additive manufacturing. Progress in Additive Manufacturing 2(4):179–191. https://doi.org/10.1007/s40964-017-0028-9
37. Lide DR (2004) CRC handbook of chemistry and physics, vol 85. CRC Press
38. Simchi A (2006) Direct laser sintering of metal powders: mechanism, kinetics and microstructural features. Mater Sci Eng A 428(1):148–158. https://doi.org/10.1016/j.msea.2006.04.117, https://www.sciencedirect.com/science/article/pii/S0921509306005491
39. Casalino G, Campanelli SL, Contuzzi N, Ludovico AD (2015) Experimental investigation and statistical optimisation of the selective laser melting process of a maraging steel. Opt Laser Technol

65:151–158. https://doi.org/10.1016/j.optlastec.2014.07.021, https://www.sciencedirect.com/science/article/pii/S0030399214002011
40. Wang D, Liu Y, Yang Y, Xiao D (2016) Theoretical and experimental study on surface roughness of 316L stainless steel metal parts obtained through selective laser melting. Rapid Prototyp J 22(4):706–716. https://doi.org/10.1108/RPJ-06-2015-0078
41. Spierings A, Herres N, Levy G (2011) Influence of the particle size distribution on surface quality and mechanical properties in AM steel parts. Rapid Prototyp J 17(3):195–202. https://doi.org/10.1108/13552541111124770
42. Yang T, Liu T, Liao W, MacDonald E, Wei H, Chen X, Jiang L (2019) The influence of process parameters on vertical surface roughness of the AlSi10Mg parts fabricated by selective laser melting. J Mater Process Technol 266:26–36. https://doi.org/10.1016/j.jmatprotec.2018.10.015, https://www.sciencedirect.com/science/article/pii/S0924013618304515
43. Pal S, Lojen G, Hudak R, Rajtukova V, Brajlih T, Kokol V, Drstvenšek I (2020) As-fabricated surface morphologies of Ti-6Al-4V samples fabricated by different laser processing parameters in selective laser melting. Addit Manuf 33:101147. https://doi.org/10.1016/j.addma.2020.101147, https://www.sciencedirect.com/science/article/pii/S221486041932336X
44. Khorasani M, Ghasemi A, Awan US, Hadavi E, Leary M, Brandt M, Littlefair G, O'Neil W, Gibson I (2020) A study on surface morphology and tension in laser powder bed fusion of Ti-6Al-4V. Int J Adv Manuf Technol 111(9):2891–2909. https://doi.org/10.1007/s00170-020-06221-w, https://doi.org/10.1007/s00170-020-06221-w
45. Dilip JJS, Zhang S, Teng C, Zeng K, Robinson C, Pal D, Stucker B (2017) Influence of processing parameters on the evolution of melt pool, porosity, and microstructures in Ti-6Al-4V alloy parts fabricated by selective laser melting. Progress in Additive Manufacturing 2(3):157–167. https://doi.org/10.1007/s40964-017-0030-2
46. Yang J, Han J, Yu H, Yin J, Gao M, Wang Z, Zeng X (2016) Role of molten pool mode on formability, microstructure and mechanical properties of selective laser melted Ti-6Al-4V alloy. Mater Des 110:558–570. https://doi.org/10.1016/j.matdes.2016.08.036, https://www.sciencedirect.com/science/article/pii/S0264127516310991
47. Verhaeghe F, Craeghs T, Heulens J, Pandelaers L (2009) A pragmatic model for selective laser melting with evaporation. Acta Materialia 57(20):6006–6012. https://doi.org/10.1016/j.actamat.2009.08.027, https://www.sciencedirect.com/science/article/pii/S1359645409005394
48. Cui X, Zhang S, Zhang CH, Chen J, Zhang JB, Dong SY (2021) Additive manufacturing of 24CrNiMo low alloy steel by selective laser melting: Influence of volumetric energy density on densification, microstructure and hardness. Mater Sci Eng A 809:140957. https://doi.org/10.1016/j.msea.2021.140957, https://www.sciencedirect.com/science/article/pii/S0921509321002264
49. Gong H, Rafi K, Gu H, Janaki Ram GD, Starr T, Stucker B (2015) Influence of defects on mechanical properties of Ti-6Al-4V components produced by selective laser melting and electron beam melting. Mater Des 86:545–554. https://doi.org/10.1016/j.matdes.2015.07.147, https://www.sciencedirect.com/science/article/pii/S0264127515302161
50. Bartolomeu F, Faria S, Carvalho O, Pinto E, Alves N, Silva FS, Miranda G (2016) Predictive models for physical and mechanical properties of Ti6Al4V produced by selective laser melting. Mater Sci Eng A 663:181–192. https://doi.org/10.1016/j.msea.2016.03.113, https://www.sciencedirect.com/science/article/pii/S092150931630329X
51. Javidrad HR, Ghanbari M, Javidrad F (2021) Effect of scanning pattern and volumetric energy density on the properties of selective laser melting Ti-6Al-4V specimens. J Mater Res Technol 12:989–998. https://doi.org/10.1016/j.jmrt.2021.03.044, https://www.sciencedirect.com/science/article/pii/S2238785421002714
52. Ladewig A, Schlick G, Fisser M, Schulze V, Glatzel U (2016) Influence of the shielding gas flow on the removal of process by-products in the selective laser melting process. Addit Manuf 10:1–9. https://doi.org/10.1016/j.addma.2016.01.004, https://www.sciencedirect.com/science/article/pii/S2214860416300161
53. Parteli EJR, Pöschel T (2016) Particle-based simulation of powder application in additive manufacturing. Powder Technol 288:96–102. https://doi.org/10.1016/j.powtec.2015.10.035, https://www.sciencedirect.com/science/article/pii/S0032591015301248
54. Metel AS, Stebulyanin MM, Fedorov SV, Okunkova AA (2019) Power density distribution for laser additive manufacturing (SLM): potential, fundamentals and advanced applications. Technologies 7(1):5. https://doi.org/10.3390/technologies7010005, https://www.mdpi.com/2227-7080/7/1/5
55. Strondl A, Lyckfeldt O, Brodin H, Ackelid U (2015) Characterization and control of powder properties for additive manufacturing. JOM 67(3):549–554. https://doi.org/10.1007/s11837-015-1304-0, https://doi.org/10.1007/s11837-015-1304-0
56. Sutton AT, Kriewall CS, Karnati S, Leu MC, Newkirk JW (2020) Characterization of AISI 304L stainless steel powder recycled in the laser powder-bed fusion process. Addit Manuf 32:100981. https://doi.org/10.1016/j.addma.2019.100981, https://www.sciencedirect.com/science/article/pii/S221486041930987X
57. Li C, Sun S, Zhang Y, Liu C, Deng P, Zeng M, Wang F, Ma P, Li W, Wang Y (2019) Effects of laser processing parameters on microstructure and mechanical properties of additively manufactured AlSi10Mg alloys reinforced by TiC. Int J Adv Manuf Technol 103(5):3235–3246. https://doi.org/10.1007/s00170-019-04001-9, https://doi.org/10.1007/s00170-019-04001-9
58. Gu D, Wang H, Chang F, Dai D, Yuan P, Hagedorn YC, Meiners W (2014) Selective laser melting additive manufacturing of TiC/AlSi10Mg bulk-form nanocomposites with tailored microstructures and properties. Phys Procedia 56:108–116. https://doi.org/10.1016/j.phpro.2014.08.153,https://www.sciencedirect.com/science/article/pii/S1875389214002983
59. Gu D, Wang H, Dai D, Chang F, Meiners W, Hagedorn YC, Wissenbach K, Kelbassa I, Poprawe R (2015) Densification behavior, microstructure evolution, and wear property of TiC nanoparticle reinforced AlSi10Mg bulk-form nanocomposites prepared by selective laser melting. J Laser Appl 27(S1):S17003
60. Zhu J, Kamiya A, Yamada T, Watazu A, Shi W, Naganuma K (2001) Effect of silicon addition on microstructure and mechanical properties of cast titanium alloys. Mater Trans 42(2):336–341. https://doi.org/10.2320/matertrans.42.336
61. Deng T, Li S, Liang Y, Sun L, Zhang Y (2020) Effects of scandium and silicon addition on the microstructure and mechanical properties of Ti-6Al-4V alloy. J Mater Res Technol 9(3):5676–5688. https://doi.org/10.1016/j.jmrt.2020.03.092, https://www.sciencedirect.com/science/article/pii/S2238785420307766
62. Lütjering G, Williams JC (2007) High temperature alloys. In: Lütjering G, Williams JC (eds) Titanium, Springer, Berlin, Heidelberg, pp 259–282. https://doi.org/10.1007/978-3-540-73036-1_6
63. Morgan AE, Broadbent EK, Ritz K, Sadana D, Burrow B (1988) Interactions of thin Ti films with Si, SiO2, Si3N4, and SiO x N y under rapid thermal annealing. J Appl Phys 64(1):344–353
64. Weavwe J, Rosenthal I (2021) Understanding anisotropic tensile properties of laser powder bed fusion additive metals: a detailed review of select examples. Advanced Manufacturing Series (NIST AMS) pp 100–44